PAPER

Check for updates

Theoretical insights into NH₃ absorption mechanisms with imidazolium-based protic ionic liquids†

Wenhui Tu,[a] Shaojuan Zeng,*[ab] Yinge Bai,[ab] Xiaochun Zhang,[a] Haifeng Dong[ab] and Xiangping Zhang [ID] *[abc]

Ionic liquids (ILs) provide a promising way for efficient absorption and separation of ammonia (NH₃) due to their extremely low vapor pressures and adjustable structures. However, the understanding of absorption mechanisms especially in terms of theoretical insights is still not very clear, which is crucial for designing targeted ILs. In this work, a universal method that integrates density functional theory and molecular dynamic simulations was proposed to study the mechanisms of NH₃ absorption by protic ionic liquids (PILs). The results showed that the NH₃ absorption performance of the imidazolium-based PILs ([BIm][X], X= Tf₂N, SCN and NO₃) is determined by not only the hydrogen bonding between the N atom in NH₃ and the protic site (H–N³) on the cation but also the cation–anion interaction. With the increase in NH₃ absorption capacity, the hydrogen bonding between [BIm][Tf₂N] and NH₃ changed from orbital dominated to electrostatic dominated, so 3.0 mol NH₃ per mol IL at 313.15 K and 0.10 MPa was further proved as a threshold for NH₃ capacity of [BIm][Tf₂N] by the Gibbs free energy results, which agrees well with the experimental results. Furthermore, the anions of [BIm][X] could also compete with NH₃ for interaction with H-N³ of the cation, which weakens the interaction between the cation and NH₃ and then decreases the NH₃ absorption ability of PILs. This study provides further understanding on NH₃ absorption mechanisms with ILs, which will guide the design of novel functionalized ILs for NH₃ separation and recovery.

1. Introduction

Ammonia (NH₃) mainly comes from various industrial emissions, such as in synthetic ammonia plants, melamine tail gas, urea granulating tower tail gas, metallurgical tail gas, and so on. The emission of NH₃ into the atmosphere causes serious environmental issues.[1–4] Therefore, the removal and recovery of NH₃ from these gases is significant to satisfy

[a] *Key Laboratory of Green Process and Engineering, Beijing Key Laboratory of Ionic Liquids Clean Process, Institute of Process Engineering, Chinese Academy of Sciences, No.1, North 2nd street, Zhongguancun, Haidian District, Beijing, 100190, China. E-mail: sjzeng@ipe.ac.cn, xpzhang@ipe.ac.cn; Fax: +86 010 82544875; Tel: +86 010 82544875*

[b] *Huizhou Institute of Green Energy and Advanced Materials, Huizhou, Guangdong, 516081, China*

[c] *College of Chemical Engineering and Environment, China University of Petroleum, Beijing, 102249, China*

† Electronic supplementary information (ESI) available: The structures and coordinates of each conformer of the ILs studied, NH₃, ILs combined with NH₃, isolated cations or anions, and anions combined with NH₃ are provided. See DOI: https://doi.org/10.1039/d2im00041e

environmental emission regulations and for resource reuse. Recently, ionic liquids (ILs) have attracted considerable attention as environmentally benign solvents for NH₃ absorption and recovery due to their peculiar properties, such as negligible vapor pressures, tunable properties and high thermal stability.[5–9] Various functionalized ILs, such as hydroxyl ILs,[10–12] metal ILs,[13–16] and protic ILs (PILs)[17,18] were reported for efficient NH₃ absorption. For instance, Shang *et al.* designed a kind of PIL with a strong hydrogen bond donating ability on cations, such as [BIm][Tf₂N] with a high NH₃ absorption capacity of 2.69 mol NH₃ (mol IL)⁻¹ at 313.15 K and 0.10 MPa, along with great selectivity and excellent recyclability.[19] Luo *et al.* also designed an efficient PIL, [2PyH][Tf₂N], by varying the cooperative hydrogen bonding, and the NH₃ absorption capacity was high—up to 3.80 mol NH₃ (mol IL)⁻¹ at 303.15 K and 0.10 MPa.[18] In addition, the elucidation of the mechanism of gas absorption is crucial for the design of targeted ILs, especially in terms of theoretical perspectives.[20,21]

In 2009, Shi *et al.* published the first work on molecular dynamic (MD) simulations of NH₃ absorption by the IL

[EMIm][Tf$_2$N]. According to the analysis of the interaction and radial distribution function of NH$_3$···cation and NH$_3$···anion, they concluded that the NH$_3$ absorption capacity of [EMIm][Tf$_2$N] is governed by the hydrogen bonding between NH$_3$ and cations.[22] Inspired by their conclusions, a series of promising ILs, such as hydroxyl ILs and PILs, were designed to absorb NH$_3$ efficiently by introducing effective sites that interact with NH$_3$, and theoretical studies were performed to verify their ideas. For example, Li *et al.* performed density functional theory (DFT) simulations to confirm that the higher NH$_3$ absorption capacity of a hydroxyl-functionalized IL than that of the analogous IL without the introduction of a hydroxyl group is mainly due to the hydrogen bonding between the hydroxyl group of the cation and the basic N atom of NH$_3$.[10] Cai *et al.* also conducted DFT simulations to verify the mechanism of NH$_3$ absorption in lithium (Li)-triethylene glycol (TEG)-chelated ILs and their results indicated that the high NH$_3$ capacity of ILs is due to the strong interaction between hydroxyl sites of the cation and NH$_3$.[23] Similarly, the DFT calculation results of our previous work[19] also indicated that NH$_3$ absorption of [BIm][Tf$_2$N] may be mainly affected by the protic hydrogen of the cation. Further, MD simulations were conducted to confirm that NH$_3$ can compete with [Tf$_2$N]$^-$ for interaction with the protic hydrogen of the cation, forming a strong hydrogen bonding.[24] So far, theoretical methods have attracted increasing attention to study the mechanism of NH$_3$ absorption with ILs.

Our previous work revealed that PILs not only show impressively high NH$_3$ absorption capacities but also their capacities are considerably affected by anions.[17,19] For instance, the capacities for NH$_3$ absorption of [BIm][Tf$_2$N], [BIm][SCN] and [BIm][NO$_3$] were 2.69, 1.96 and 1.30 mol NH$_3$ (mol IL)$^{-1}$ at 313.15 K and 0.10 MPa, respectively, as shown in Table 1. However, the mechanism is not clear. Here, DFT and MD simulations were conducted to further study the NH$_3$ absorption mechanism by [BIm]$^+$-based PILs to reveal the essence of the interaction between ILs and NH$_3$, as well as the effect of anions on NH$_3$ capacity. The comprehensive theoretical studies not only complement deeper understanding on NH$_3$ absorption mechanisms by the PILs but also provide a guideline to design new efficient ILs.

2. Results and discussion

2.1 The interaction between NH$_3$ and [BIm][Tf$_2$N]

The optimized structures that illustrate [BIm][Tf$_2$N] interacting with one, two, three and four NH$_3$ molecules are demonstrated in Fig. 2. The results showed that the NH$_3$
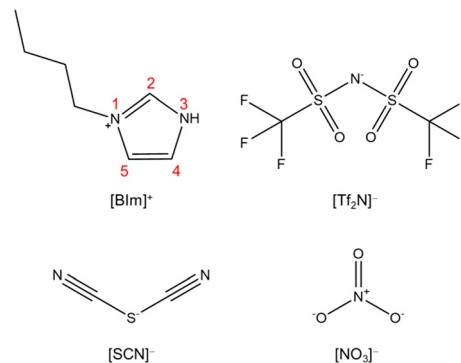

Fig. 1 Structures of the cation and anions studied in this work.

molecule mainly interacts with the site of protic hydrogen (H–N^3, the atom labels are provided in Fig. 1) of [BIm][Tf$_2$N] *via* hydrogen bonding. For example, the distance between N of the 1st NH$_3$ and H of H–N^3 was 1.7 Å (Fig. 2a), which is less than the sum of the van der Walls radii of N and H atoms.[25] On the other hand, hydrogen bonding was also discovered between NH$_3$ and the anion [Tf$_2$N]$^-$, as shown in Fig. 2a–d. For [BIm][Tf$_2$N]···NH$_3$, the interaction energy (ΔE) between the PIL and NH$_3$ was −17.30 kcal mol^{-1} when the NH$_3$ was located around H–N^3 (Fig. 2a), which is almost twice as those of NH$_3$ interacting with H–C$^{2/4/5}$ (see Fig. S1†). For [BIm][Tf$_2$N]···2NH$_3$, the most stable structure was obtained when the 2nd NH$_3$ molecule connected to the 1st NH$_3$ molecule (see Fig. 2b). The ΔE between the IL and two NH$_3$ molecules was −27.30 kcal mol^{-1}, implying that the ΔE for the 2nd NH$_3$ molecule was −10.00 kcal mol^{-1}. Interestingly, the distance between the N atom of the 1st NH$_3$ molecule and H–N^3 decreased from 1.7 Å to 1.6 Å while the 2nd NH$_3$ molecule was absorbed. In other words, the hydrogen bonding formed between the 1st NH$_3$ molecule and H–N^3 was enhanced. A similar phenomenon was discovered from the interactions between H$_2$O molecules and [EIm][Tf$_2$N], which means that the distance between the O atom of the 1st H$_2$O molecule and H–N^3 of [EIm]$^+$ is shortened when the 2nd H$_2$O molecule interacts with the 1st H$_2$O molecule.[26]

The structures of [BIm][Tf$_2$N] interacting with three and four NH$_3$ molecules are demonstrated in Fig. 2c and d, respectively. It was found that the rest of NH$_3$ molecules can interact with the 1st absorbed NH$_3$ molecule. It is worth noting that the calculated ΔE of absorption of the 1st and 2nd NH$_3$ molecules is much larger than that of the 3rd and 4th NH$_3$ molecules, *i.e.*, −17.30 and −10.00 kcal mol^{-1} *versus* −4.60 and −5.70 kcal mol^{-1}. The findings revealed that the 1st and 2nd NH$_3$ molecules are absorbed *via* different types of interactions compared to the 3rd and 4th NH$_3$ molecules.

Table 1 The viscosities, densities and NH$_3$ capacities at 313.15 K and 0.10 MPa of the PILs[17]

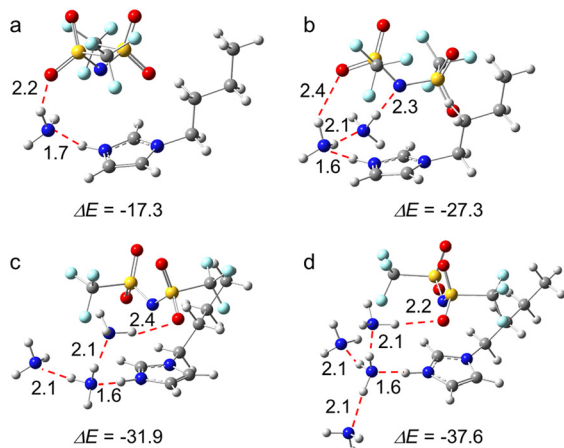| ILs	Viscosity (mPa s)	Density (g L^{-1})	NH$_3$ capacity (mol NH$_3$ (mol IL)$^{-1}$)
[BIm][Tf$_2$N]	47.14	1460.24	2.69
[BIm][SCN]	84.30	1078.66	1.96
[BIm][NO$_3$]	136.95	1165.50	1.30

Fig. 2 The optimized structures of [BIm][Tf$_2$N] with (a) one, (b) two, (c) three, and (d) four NH$_3$ molecules. (Color of ligand: N, blue; H, gray; C, dark gray; S, yellow; O, red; F, pale turquoise. All the distances are given in Å. $\Delta E = E(\text{IL}\cdots n\text{NH}_3) - E(\text{IL}) - n \times E(\text{NH}_3)$).

Fig. 3 The EDA results at the M062X/TZP level of theory for each step of [BIm][Tf$_2$N] to capture one NH$_3$. The numbers on the lines indicate the changes of values of adjacent two points, and their colours are consistent with the lines.

The former two are through strong hydrogen bonding while the latter two are dominated by VdW interactions. The essence of these interactions was further analyzed *via* energy decomposition analysis (EDA), and detailed discussions are given in the next sections.

2.2 Energy decomposition analysis of NH$_3$ absorption with [BIm][Tf$_2$N]

In order to present a quantitative interpretation and more details of the interactions between [BIm][Tf$_2$N] and NH$_3$, EDA was performed. Within the EDA scheme, the total interaction energy consists of three meaningful physical terms, namely, the repulsive exchange (Pauli) interaction ΔE_{Pauli}, the electrostatic interaction ΔE_{elstat} and the orbital interaction ΔE_{orb}, which includes the orbital relaxation and orbital mixing between the fragments.[27,28] In addition, the summation of Pauli repulsion and electrostatic interactions is often defined as the steric interaction ΔE_{steric}, which arises from the fact that each atom in a molecule occupies a certain amount of space. The total and the individual interactions of the process for each NH$_3$ absorbed by [BIm][Tf$_2$N] are given in Table 2 and Fig. 3. The results showed that the interactions between the 1st and 2nd NH$_3$ molecules with [BIm][Tf$_2$N] are considerable, especially for the 1st NH$_3$
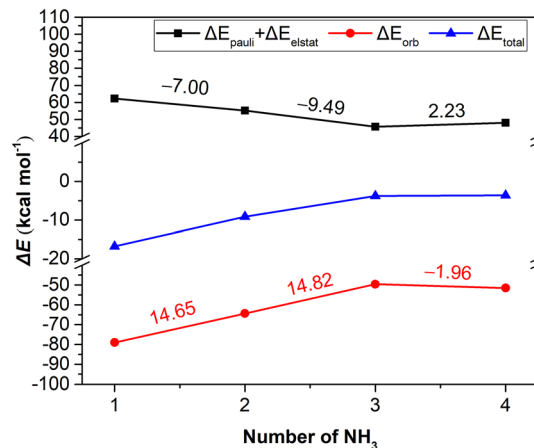
molecule, and its total interaction energy is as high as −16.79 kcal mol^{-1}. However, the total interaction energies of the 3rd and 4th NH$_3$ molecules are much lower than those of the 1st and 2nd NH$_3$ molecules, which are around −3.50 kcal mol^{-1}. The 3rd NH$_3$ molecule is favored by electrostatic interactions of 8.16 kcal mol^{-1} compared to the 4th NH$_3$ molecule. This is most likely because the 3rd NH$_3$ molecule interacts with the anion through hydrogen bonding (see Fig. 2c).

The plots in Fig. 3 demonstrate that the orbital interaction is more likely to decay than the steric interaction. For example, the orbital interaction decreased by 14.65 kcal mol^{-1} from the 1st to the 2nd NH$_3$ molecule, while the corresponding steric interactions only decreased by 7.00 kcal mol^{-1}. The results indicated that the orbital interaction makes a great contribution to the total interaction. However, in the case of the 4th NH$_3$ molecule, the changes of ΔE_{steric} and ΔE_{orb} were small compared to those of the 3rd NH$_3$ molecule, which is most likely due to physical interaction of the 4th NH$_3$ molecule. In this case, the electrostatic interaction plays the most important role.

2.3 Gibbs free energy of NH$_3$ absorption with [BIm][Tf$_2$N]

Our previous experimental results[16] showed that the NH$_3$ absorption capacity of [BIm][Tf$_2$N] is 2.69 mol NH$_3$ (mol

Table 2 EDA at the M062X/TZP level for each step ([BIm][Tf$_2$N]$\cdots$(i-1) NH$_3$ + NH$_3$ →[BIm][Tf$_2$N]$\cdots i$NH$_3$, i = 1–4) of [BIm][Tf$_2$N] to capture one NH$_3$ molecule, and all the energies are expressed in kcal mol^{-1}

Interaction energies[a]	1st NH$_3$	2nd NH$_3$	3rd NH$_3$	4th NH$_3$
ΔE_{Pauli}	+92.02	+72.05	+61.64	+55.71
ΔE_{elstat}	−29.76	−16.79	−15.87	−7.71
ΔE_{steric} ($\Delta E_{\text{Pauli}} + \Delta E_{\text{elstat}}$)	+62.26	+55.26	+45.77	+48.00
ΔE_{orb}	−79.05	−64.40	−49.58	−51.54
ΔE_{total}	−16.79	−9.14	−3.81	−3.54

^{a} $\Delta E = E(\text{IL}\cdots n\text{NH}_3) - E(\text{IL}\cdots (n\text{-}1)\text{NH}_3) - E(\text{NH}_3)$.

IL)$^{-1}$, which is close to 3.0 mol NH$_3$ (mol IL)$^{-1}$ at 313.15 K and 0.10 MPa. The high capacity for NH$_3$ of [BIm][Tf$_2$N] was probably attributed to the strong hydrogen bonding site H–N^3 in the [BIm]$^+$ cation. Here, we revisited this open question by computing the Gibbs free energy (ΔG) for [BIm][Tf$_2$N] absorption of different moles of NH$_3$ molecules. The calculated ΔG values are shown in Fig. 4, and their values are highlighted in red. The ΔG values for [BIm][Tf$_2$N] absorbing one and two moles NH$_3$ were −3.6 and −3.1 kcal mol^{-1}, respectively. These two negative values indicated that the process of [BIm][Tf$_2$N] absorbing one or two moles NH$_3$ takes place spontaneously and easily.

The ΔG value for [BIm][Tf$_2$N] absorbing three moles NH$_3$ was 1.8 kcal mol^{-1}. This slightly positive value reveals that the absorption of three moles NH$_3$ by [BIm][Tf$_2$N] is thermodynamically feasible. Moreover, the other conformers of [BIm][Tf$_2$N]···3NH$_3$ are shown in Fig. S3.† The relative energies (E_r), ΔG values and Boltzmann distribution weighting factors (w_i) are summarized in Table S1.† The results indicated that most of the conformers have comparable E_r values and their ΔG values are close to zero as well. It should be noted that the most stable structure of [BIm][Tf$_2$N]···3NH$_3$ (Fig. S3a†) is slightly more stable than the structure in Fig. 2c (equal to Fig. S3d†). The energy of the former was 1.1 kcal mol^{-1} lower than the latter. Moreover, the most stable structure was dominant among the displayed conformers with a w_i value of 0.432, and its corresponding ΔG value was −0.05 kcal mol^{-1}. The result indicated that [BIm][Tf$_2$N] is capable of absorbing close to 3 moles NH$_3$ in consideration of thermodynamics. It is also consistent with the experimental fact that the NH$_3$ capacity of H–C^2 is less than 1.0 mol NH$_3$ (mol IL)$^{-1}$.[5,6,17]

We also calculated the ΔG value for the [BIm][Tf$_2$N] ···4NH$_3$ system. The DFT calculations yielded a large positive value of 6.7 kcal mol^{-1} for the hypothetical process, indicating that [BIm][Tf$_2$N] failed to absorb 4 moles NH$_3$ spontaneously at 313.15 K and 0.10 MPa. Furthermore, the energy of the most stable structure of [BIm][Tf$_2$N]···4NH$_3$ (Fig. S4a†) was 3.8 kcal mol^{-1} lower than that of the structure shown in Fig. 2d (equal to Fig. S4t†), but the ΔG value of [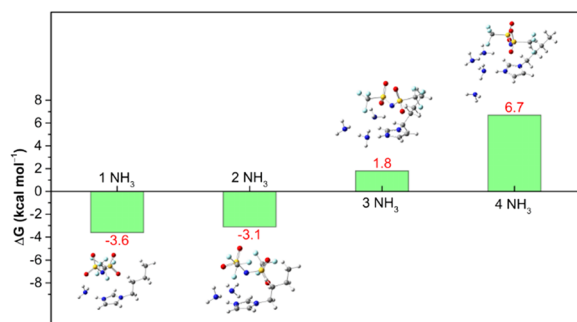BIm][Tf$_2$N] absorbed 4 moles NH$_3$ molecules based on the most stable structure of [BIm][Tf$_2$N]···4NH$_3$ (2.5 kcal mol^{-1}), which indicated that this structure is also unfavorable from a thermodynamic point of view.

2.4 The interaction between anions and NH$_3$

Based on the above analysis, it was concluded that H–N^3 plays an important role in NH$_3$ absorption of [BIm][Tf$_2$N]. However, the experimental results (see Table 1) also indicated that the anions have an observable influence on NH$_3$ capacity of PILs. To reveal the possible mechanisms, the interactions between anions and NH$_3$ were also studied by DFT calculations. As seen in Fig. 5, all the anions interacted with NH$_3$ via hydrogen bonding. The interaction energy between [NO$_3$]$^-$ and NH$_3$ was the largest one among them, while the difference of interaction energies was less than 3.0 kcal mol^{-1}. Although the anion [Tf$_2$N]$^-$ offered more hydrogen bond acceptors than the other two anions, it seemed impossible to cause such a great difference in NH$_3$ capacity of PILs (NH$_3$ capacity of [BIm][Tf$_2$N] is almost twice that of [BIm][NO$_3$] in Table 1). Furthermore, in terms of interaction energies, [BIm][NO$_3$] should show a more likely higher NH$_3$ capacity than [BIm][SCN], which conflicts with experimental results. In sum, the interaction between NH$_3$ and anions is not the direct reason that affects NH$_3$ absorption capacity of PILs.

2.5 The interaction between cations and anions

The H–N^3 site is a main hydrogen bond donor that interacts with NH$_3$, and then the anions may also provide hydrogen bond acceptors to form hydrogen bonding with the protic site, therefore influencing the NH$_3$ absorption capacity of PILs. In order to verify this assumption, DFT calculations were conducted to study the interactions between cations and anions. The most stable structures for these three "ion pairs" of [BIm][Tf$_2$N], [BIm][SCN] and [BIm][NO$_3$] are depicted in Fig. 6. In addition, the interaction energies between cations and anions are indicated as well (the detailed values are in Fig. S10†). It was found that all the anions prefer to interact with H–N^3, meaning that the anions compete against NH$_3$ for H–N^3. It was implied that the stronger interaction between cations and anions results in a lower NH$_3$ absorption capacity. As seen in Fig. 6, the interaction

Fig. 4 ΔG of [BIm][Tf$_2$N] + iNH$_3$ → [BIm][Tf$_2$N]···iNH$_3$, (i = 1–4) calculated at the M062X/def2TZVP level, including the B3LYP/6-31 + G* thermodynamic correction.

Fig. 5 The optimized structures of NH$_3$ interact with (a) [Tf$_2$N]$^-$, (b) [SCN]$^-$ and (c) [NO$_3$]$^-$ (color of ligand: N, blue; H, gray; C, dark gray; S, yellow; O, red; F, pale turquoise).

© 2023 The Author(s). Co-published by the Institute of Process Engineering, Chinese Academy of Sciences and the Royal Society of Chemistry

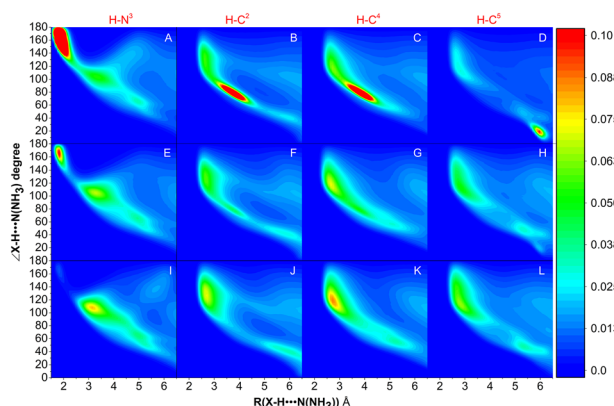*Ind. Chem. Mater.*, 2023, **1**, 262–270 | **265**

Fig. 6 The interaction energies between cations and anions of PILs. A more negative value indicates a stronger interaction (color of ligand: N, blue; H, gray; C, dark gray; S, yellow; O, red; F, pale turquoise).

energies between the cations and anions of these PILs followed the order $[BIm][Tf_2N] < [BIm][SCN] < [BIm][NO_3]$. Moreover, the increasing interaction between cations and anions would decrease the free volume in PILs that accommodates NH_3, decreasing the NH_3 capacity of PILs.[29] Therefore, the reason for the anions influencing NH_3 capacity of PILs originates from the strength of interaction between anions and cations.

2.6 The distribution of hydrogen bonding around $[BIm]^+$

The MD simulations of NH_3 absorption of ILs were further carried out to study the distribution of NH_3 and anions in PILs. Fig. 7 shows the combined distribution functions of $\angle X–H\cdots N(NH_3)$ *versus* the distance between the H atom of the cation and the N atom of NH_3 ($R_{H\cdots N(NH_3)}$). X refers to C

(*i.e.*, C2-site, C4-site, and C5-site, indicated as C^2, C^4, and C^5, respectively) and N (*i.e.*, N^3-site, indicated as N^3) atoms on the imidazolium ring of $[BIm]^+$. It was found that NH_3 molecules are mainly distributed around $H–N^3$ in $[BIm][Tf_2N]$ (with a large region in red color, panel A). In panel A, the red region represented the range where $130° < \angle N–H\cdots N(NH_3) < 180°$ and $1.5 \text{ Å} < R_{H\cdots N(NH_3)} < 2.0 \text{ Å}$, which indicated that most of the NH_3 molecules interact with $H–N^3$ by strong hydrogen bonding. A similar red region was also found in panel E, but its area was much less than that of $[BIm][Tf_2N]$. It was demonstrated that part of NH_3 molecules distribute around $H–N^3$ in $[BIm][SCN]$ by strong hydrogen bonding. However, it was hard to find any red region in panel I, which means that few NH_3 molecules distribute around $H–N^3$ in $[BIm][NO_3]$ by strong hydrogen bonding. In addition, regions with red color were also found in panels B–D. These are possible indications that $H–C^2$, $H–C^4$, and $H–C^5$ are sharing part of NH_3 molecules around $H–N^3$.

2.7 The distribution of anions around the $[BIm]^+$ cation

To study the distribution of anions around $H–N^3$ of the cation, the radial distribution functions (RDFs) before and after NH_3 absorption of $H–N^3$(cation)$\cdots$N/C(anion) and the three-dimensional probability distribution of NH_3, and the anions around the $[BIm]^+$ cation in PILs after NH_3 absorption were calculated as shown in Fig. 8 and 9, respectively. The results showed that the distance of the first evident peak of RDFs for the three PILs follows the order $[BIm][NO_3] < [BIm][SCN] < [BIm][Tf_2N]$. The $[NO_3]^-$ anions were organized closer, and more $[SCN]^-$ anions were around $H–N^3$, which leads to a smaller probability for NH_3 molecules interacting with $H–N^3$ in $[BIm][NO_3]$ and a lower NH_3 capacity. However, for the $[Tf_2N]^-$ anion, it was the most far away from $H–N^3$ among the three anions.
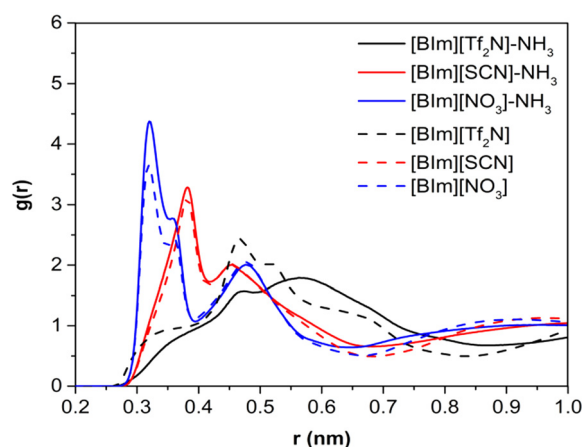

Fig. 7 Combined distribution functions of $\angle N/C–H\cdots N(NH_3)$ *versus* the distance of $H\cdots N(NH_3)$ between the cation and NH_3. The first column of panels A, F, and H reflects the distribution of NH_3 around $H–N^3$. The 2nd to 4th columns of the panels reflect the distribution of NH_3 around $H–C^2$, $H–C^4$, and $H–C^5$, respectively. Panels A–D, E–H and I–L are combined distribution functions for NH_3 absorption by $[BIm][Tf_2N]$, $[BIm][SCN]$ and $[BIm][NO_3]$, respectively.

Fig. 8 RDF presentation between the H atom of $H–N^3$ in $[BIm]^+$ and the central atom in anions (the N atom is assigned as the central atom for $[Tf_2N]^-$ and $[NO_3]^-$, and the C atom is assigned as the central atom for $[SCN]^-$).
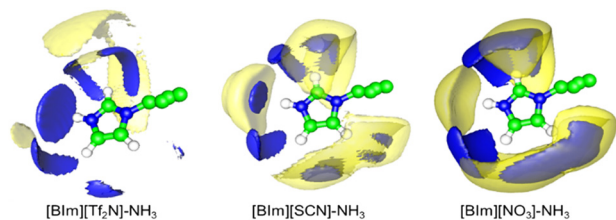
Fig. 9 Three-dimensional probability distribution of NH_3 (blue) and anions (yellow) around $[BIm]^+$ in the bulk liquid of ILs after NH_3 absorption. In each case, the blue and yellow surfaces are drawn at 4 times the average density of the corresponding NH_3 or anions in the bulk region.

Consequently, $[BIm][Tf_2N]$ provided more opportunities for $H-N^3$ to attract NH_3 and more free volume to accommodate NH_3.[30,31] Interestingly, the RDFs of $[BIm][Tf_2N]$ before and after NH_3 absorption exhibited more evident changes than those of the other two PILs. This is likely because the $[Tf_2N]^-$ anion has the largest size among these three anions, so it is vulnerable to be attacked by NH_3 resulting in considerable spatial displacement. Fig. 8 also shows that the anion $[Tf_2N]^-$ keeps away from $H-N^3$ in the bulk phase of $[BIm][Tf_2N]$ with NH_3 absorption compared to the bulk phase without NH_3 absorption.

3. Conclusions

In this work, both DFT calculations and MD simulations were conducted to deeply understand the mechanisms of NH_3 absorption with PILs, including $[BIm][Tf_2N]$, $[BIm][SCN]$ and $[BIm][NO_3]$, in terms of theoretical insights. The interactions between $[BIm][Tf_2N]$ and NH_3, anions and NH_3, cations and anions, and the NH_3 distribution around $H-N^3$ and $H-C^{2/4/5}$ in $[BIm]^+$, as well as the anion organization around $H-N^3$ before and after NH_3 absorption for the three PILs, were systematically investigated. The results indicated that both the strong hydrogen bonding between NH_3 and $H-N^3$ of the cation and the weak interaction between cations and anions lead to a high NH_3 capacity of the PILs. Moreover, the orbital moiety of the total interaction between NH_3 and $[BIm][Tf_2N]$ decays dramatically with the increase of NH_3 absorption, and the major part changed from orbital to electrostatic, which further proved that 3.0 mol NH_3 (mol IL)$^{-1}$ is a threshold for the NH_3 capacity of $[BIm][Tf_2N]$. On the other hand, the anions of the PILs could also compete with NH_3 for interaction with $H-N^3$ of the cations, when the interaction between the cations and anions became stronger, the corresponding anions would prefer to gather near or around the $H-N^3$ of the cation and decreased the probability of $H-N^3$ to interact with NH_3, thus reducing the NH_3 absorption capacity of the PILs. This study provides a deep understanding of the mechanism of NH_3 absorption with ILs, which will guide the design of novel functionalized ILs for NH_3 separation and recovery applications.

4. Computational details

4.1 Density functional theory (DFT) calculations

The structures of PILs and PIL-NH_3 were first optimized at the B3LYP/6-31 + G* theoretical level in consideration of solvation *via* polarizable continuum mode (PCM),[32] together with the employment of the DFT-D3 approach to consider the interaction of dispersion.[33] Frequency analyses were performed at the same level to confirm the optimized structures: no imaginary frequencies were found for the local minima. Then single point calculations were conducted for optimized structures at the M062X/def2-TZVP level to obtain the energy in the ideal gas phase. The zero point energies (ZPE) were obtained from the frequency calculation at the B3LYP-D3/6-31 + G* level. When applying PCM, the solvent parameters of ILs are necessary. The dielectric constant and refractive index of the ILs studied were estimated to be 15.0 and 1.43, respectively, based on published works.[34–36] All the above calculations were performed by employing the Gaussian09 package.[37] The Amsterdam density functional (ADF) suite of programs was employed to perform energy decomposition analysis (EDA).[38,39] EDA was conducted *via* single point calculations at the M062X level with an all-electron basis set of TZP quality.[40]

The interaction energy (ΔE), which is the change in energy between the complex and its monomers, was calculated using eqn (1):

$$\Delta E = E(A\cdots B) - E(A) - E(B) \qquad (1)$$

where $E(A)$, $E(B)$ and $E(A\cdots B)$ are the ideal gas phase electronic energies of A, B and $A\cdots B$, respectively.

The final Gibbs energy (G) in solution included two parts, *i.e.*, the ideal gas phase electronic energy (E) and the gas phase thermostatistical contribution (G_{RROH}) (see eqn (2)).

$$G = E + G_{RROH} \qquad (2)$$

The change in Gibbs energy (ΔG) for a process can be calculated by eqn (3):

$$\Delta G = \Delta E + \Delta G_{RROH} \qquad (3)$$

The thermostatistical contribution is calculated as follows:

$$G_{RROH} = ZPE + E_{therm} + PV - TS \qquad (4)$$

where ZPE is the zero point vibrational energy, E_{therm} is the thermal energy, and P, V, T, and S denote the pressure, volume, temperature and entropy, respectively. T and P were set to 313.15 K and 0.10 MPa, respectively.

4.2 Molecular dynamic (MD) calculations

All the MD simulations were performed using the GROMACS simulation package[41] at 313.15 K and 0.10 MPa. The time step was set to 2 fs and the velocity-Verlet algorithm was used

to integrate the equations of motion. All the covalent bonds were constrained using the LINCS algorithm. A cutoff of 1.2 nm was set for both the LJ and Coulombic interactions. The LJ tail correction was added to the energy and pressure, and long-range electrostatic interactions were calculated using the particle-mesh Ewald (PME) method.[42] Cross interactions between different atom types were computed using standard Lorentz–Berthelot rules. The temperature was controlled using a Nosé–Hoover thermostat with a coupling time constant of 0.2 ps and the pressure was maintained using a Parrinello–Rahman barostat with a coupling time of 2.0 ps. Periodic boundary conditions were applied in all directions.

The initial configurations were built with the PACKMOL package[43] by randomly disposing 1000 ILs for pure IL systems and 1000 ILs + m NH$_3$ (m = 3000, 2000, 1500 for [BIm][Tf$_2$N], [BIm][SCN] and [BIm][NO$_3$], respectively) molecules. The force field values of the ILs were obtained from the literature,[44–47] and the NH$_3$ molecule was modelled using the OPLS-AA force field.[48] Due to the low-diffusion of ILs, the system was heated up to 500 K for 10 ns to keep the ion mobility. The temperature was gradually decreased to 313.15 K. The production run of 100 ns was carried out in an NPT ensemble, and structure analysis was conducted based on the last 50 ns.

Abbreviation

[BIm][Tf$_2$N]	1-Butyl-imidazolium bis(trifluoromethylsulfonyl)imide
[2PyH][Tf$_2$N]	2-Aminopyridinium bis(trifluoromethylsulfonyl)imide
[EMIm][Tf$_2$N]	1-Ethyl-3-methylimidazolium bis(trifluoromethylsulfonyl)imide
[BMIm][Tf$_2$N]	1-Butyl-3-methylimidazolium bis(trifluoromethylsulfonyl)imide
[BMIm][SCN]	1-Butyl-3-methylimidazolium thiocyanide
[BMIm][DCA]	1-Butyl-3-methylimidazolium dicyandiamide
[EIm][Tf$_2$N]	1-Ethyl-imidazolium bis(trifluoromethylsulfonyl)imide

Conflicts of interest

The authors declare no conflict of interest.

Acknowledgements

References

1 J. J. Gao, K. Wang, Y. Wang, S. H. Liu, C. Y. Zhu, J. M. Hao, H. J. Liu, S. B. Hua and H. Z. Tian, Temporal-spatial characteristics and source apportionment of PM2.5 as well as its associated chemical species in the Beijing-Tianjin-Hebei region of China, *Environ. Pollut.*, 2018, **233**, 714–724.

2 Z. X. Wang, L. W. Wang, P. Gao, Y. Yu and R. Z. Wang, Analysis of composite sorbents for ammonia storage to eliminate NO$_x$ emission at low temperatures, *Appl. Therm. Eng.*, 2018, **128**, 1382–1390.

3 P. J. He, S. Y. Wei, L. M. Shao and F. Lu, Emission potential of volatile sulfur compounds (VSCs) and ammonia from sludge compost with different bio-stability under various oxygen levels, *Waste Manage.*, 2018, **73**, 113–122.

4 S. Zeng, Y. Cao, P. Li, X. Liu and X. Zhang, Ionic liquid-based green processes for ammonia separation and recovery, *Curr. Opin. Green Sustainable Chem.*, 2020, **25**, 100354.

5 A. Yokozeki and M. B. Shiflett, Vapor-liquid equilibria of ammonia plus ionic liquid mixtures, *Appl. Energy*, 2007, **84**, 1258–1273.

6 A. Yokozeki and M. B. Shiflett, Ammonia solubilities in room-temperature ionic liquids, *Ind. Eng. Chem. Res.*, 2007, **46**, 1605–1610.

7 Z. Lei, C. Dai and B. Chen, Gas solubility in ionic liquids, *Chem. Rev.*, 2014, **114**, 1289–1326.

8 H. Qin, X. Hu, J. Wang, H. Cheng, L. Chen and Z. Qi, Overview of acidic deep eutectic solvents on synthesis, properties and applications, *Green Energy Environ.*, 2020, **5**, 8–21.

9 H. Qin, Z. Song, H. Cheng, L. Deng and Z. Qi, Physical absorption of carbon dioxide in imidazole-PTSA based deep eutectic solvents, *J. Mol. Liq.*, 2021, **326**, 115292.

10 Z. Li, X. Zhang, H. Dong, X. Zhang, H. Gao, S. Zhang, J. Li and C. Wang, Efficient absorption of ammonia with hydroxyl-functionalized ionic liquids, *RSC Adv.*, 2015, **5**, 81362–81370.

11 J. Palomar, M. Gonzalez-Miquel, J. Bedia, F. Rodriguez and J. J. Rodriguez, Task-specific ionic liquids for efficient ammonia absorption, *Sep. Purif. Technol.*, 2011, **82**, 43–52.

12 J. Lemus, J. Bedia, C. Moya, N. Alonso-Morales, M. A. Gilarranz, J. Palomar and J. J. Rodriguez, Ammonia capture from the gas phase by encapsulated ionic liquids (ENILs), *RSC Adv.*, 2016, **6**, 61650–61660.

13 S. Zeng, L. Liu, D. Shang, J. Feng, H. Dong, Q. Xu, X. Zhang and S. Zhang, Efficient and reversible absorption of ammonia by cobalt ionic liquids through Lewis acid–base and cooperative hydrogen bond interactions, *Green Chem.*, 2018, **20**, 2075–2083.

14 F. T. Kohler, S. Popp, H. Klefer, I. Eckle, C. Schrage, B. Böhringer, D. Roth, M. Haumann and P. Wasserscheid, Supported ionic liquid phase (SILP) materials for removal of hazardous gas compounds–efficient and irreversible NH$_3$ adsorption, *Green Chem.*, 2014, **16**, 3560–3568.

15 W. Chen, S. Liang, Y. Guo, X. Gui and D. Tang, Investigation on vapor–liquid equilibria for binary systems of metal ion-containing ionic liquid [bmim]Zn$_2$Cl$_5$/NH$_3$ by experiment and modified UNIFAC model, *Fluid Phase Equilib.*, 2013, **360**, 1–6.

16 A. Kaftan, H. Klefer, M. Haumann, M. Laurin, P. Wasserscheid and J. Libuda, An operando DRIFTS-MS study of NH$_3$ removal by supported ionic liquid phase (SILP) materials, *Sep. Purif. Technol.*, 2017, **174**, 245–250.

17 D. W. Shang, L. Bai, S. J. Zeng, H. F. Dong, H. S. Gao, X. P. Zhang and S. J. Zhang, Enhanced NH$_3$ capture by imidazolium-based protic ionic liquids with different anions and cation substituents, *J. Chem. Technol. Biotechnol.*, 2018, **93**, 1228–1236.

18 X. Y. Luo, R. X. Diu, X. Y. Chen, B. Y. Pei, J. Q. Li and C. M. Wang, Reversible construction of ionic networks through cooperative hydrogen bonds for efficient ammonia absorption, *ACS Sustainable Chem. Eng.*, 2019, **7**, 9888–9895.

19 D. W. Shang, X. P. Zhang, S. J. Zeng, K. Jiang, H. S. Gao, H. F. Dong, Q. Y. Yang and S. J. Zhang, Protic ionic liquid [Bim][NTf$_2$] with strong hydrogen bond donating ability for highly efficient ammonia absorption, *Green Chem.*, 2017, **19**, 937–945.

20 J. Ruan, X. Ye, R. Wang, L. Chen, L. Deng and Z. Qi, Experimental and theoretical study on efficient CO$_2$ absorption coordinated by molecules and ions of DBN and 1, 2, 4-triazole formed deep eutectic solvents, *Fuel*, 2023, **334**, 126709.

21 J. Tian and B. Liu, Ammonia capture with ionic liquid systems: A review, *Crit. Rev. Environ. Sci. Technol.*, 2022, **52**, 767–809.

22 W. Shi and E. J. Maginn, Molecular simulation of ammonia absorption in the ionic liquid 1-ethyl-3-methylimidazolium bis(trifluoromethylsulfonyl)imide ([emim][Tf$_2$N]), *AIChE J.*, 2009, **55**, 2414–2421.

23 Z. Cai, J. Zhang, Y. Ma, W. Wu, Y. Cao, K. Huang and L. Jiang, Chelation-activated multiple-site reversible chemical absorption of ammonia in ionic liquids, *AIChE J.*, 2022, **68**, e17632.

24 T. Zhao, S. Zeng, Y. Li, Y. Bai, L. Bai, W. Li, X. Zhang and S. Zhang, Molecular insight into the effect of ion structure and interface behavior on the ammonia absorption by ionic liquids, *AIChE J.*, 2022, **68**, e17860.

25 A. V. Bondi, van der Waals volumes and radii, *J. Phys. Chem.*, 1964, **68**, 441–451.

26 H. E. Bailey, Y. L. Wang and M. D. Fayer, Impact of hydrogen bonding on the dynamics and structure of protic ionic liquid/water binary mixtures, *J. Phys. Chem. B*, 2017, **121**, 8564–8576.

27 M. von Hopffgarten and G. Frenking, Energy decomposition analysis, *Wiley Interdiscip. Rev.: Comput. Mol. Sci.*, 2012, **2**, 43–62.

28 L. Liu, E. Osorio and T. Heine, The importance of dynamics studies on the design of sandwich structures: a CrB$_{24}$ case, *Phys. Chem. Chem. Phys.*, 2016, **18**, 18336–18341.

29 G. B. Damas, A. B. A. Dias and L. T. Costa, A quantum chemistry study for ionic liquids applied to gas capture and separation, *J. Phys. Chem. B*, 2014, **118**, 9046–9064.

30 A. R. Shaikh, H. Karkhanechi, E. Kamio, T. Yoshioka and H. Matsuyama, Quantum mechanical and molecular dynamics simulations of dual-amino-acid ionic liquids for CO$_2$ capture, *J. Phys. Chem. C*, 2016, **120**, 27734–27745.

31 F. J. Liu, W. Chen, J. X. Mi, J. Y. Zhang, X. Kan, F. Y. Zhong, K. Huang, A. M. Zheng and L. L. Jiang, Thermodynamic and molecular insights into the absorption of H$_2$S, CO$_2$, and CH$_4$ in choline chloride plus urea mixtures, *AIChE J.*, 2019, **65**, e16574.

32 S. Miertus, E. Scrocco and J. Tomasi, Electrostatic interaction of a solute with a continuum. A direct utilizaion of AB initio molecular potentials for the prevision of solvent effects, *Chem. Phys.*, 1981, **55**, 117–129.

33 S. Grimme, J. Antony, S. Ehrlich and H. Krieg, A consistent and accurate ab initio parametrization of density functional dispersion correction (DFT-D) for the 94 elements H-Pu, *J. Chem. Phys.*, 2010, **132**, 154104.

34 V. S. Bernales, A. V. Marenich, R. Contreras, C. J. Cramer and D. G. Truhlar, Quantum mechanical continuum solvation models for ionic liquids, *J. Phys. Chem. B*, 2012, **116**, 9122–9129.

35 X. Wang, S. Zhang, J. Yao and H. Li, The polarity of ionic liquids: relationship between relative permittivity and spectroscopic parameters of probe, *Ind. Eng. Chem. Res.*, 2019, **58**, 7352–7361.

36 M. M. Huang, Y. P. Jiang, P. Sasisanker, G. W. Driver and H. Weingartner, Static relative dielectric permittivities of ionic liquids at 25 °C, *J. Chem. Eng. Data*, 2011, **56**, 1494–1499.

37 M. J. Frisch, G. W. Trucks, H. B. Schlegel, G. E. Scuseria, M. A. Robb, J. R. Cheeseman, G. Scalmani, V. Barone, G. A. Petersson, H. Nakatsuji, X. Li, M. Caricato, A. Marenich, J. Bloino, B. G. Janesko, R. Gomperts, B. Mennucci, H. P. Hratchian, J. V. Ortiz, A. F. Izmaylov, J. L. Sonnenberg, D. Williams-Young, F. Ding, F. Lipparini, F. Egidi, J. Goings, B. Peng, A. Petrone, T. Henderson, D. Ranasinghe, V. G. Zakrzewski, J. Gao, N. Rega, G. Zheng, W. Liang, M. Hada, M. Ehara, K. Toyota, R. Fukuda, J. Hasegawa, M. Ishida, T. Nakajima, Y. Honda, O. Kitao, H. Nakai, T. Vreven, K. Throssell, J. A. Montgomery, Jr., J. E. Peralta, F. Ogliaro, M. Bearpark, J. J. Heyd, E. Brothers, K. N. Kudin, V. N. Staroverov, T. Keith, R. Kobayashi, J. Normand, K. Raghavachari, A. Rendell, J. C. Burant, S. S. Iyengar, J. Tomasi, M. Cossi, J. M. Millam, M. Klene, C. Adamo, R. Cammi, J. W. Ochterski, R. L. Martin, K. Morokuma, O. Farkas, J. B. Foresman and D. J. Fox, *Gaussian 09, Revision D.01*, Gaussian Inc., Wallingford CT, 2013.

38 G. te Velde, F. M. Bickelhaupt, E. J. Baerends, C. F. Guerra, S. J. A. Van Gisbergen, J. G. Snijders and T. Ziegler, Chemistry with ADF, *J. Comput. Chem.*, 2001, **22**, 931–967.

39 M. Du, C. Dai, A. Chen, X. Wu, Y. Li, Y. Liu, W. Li and M. Zhao, Investigation on the aggregation behavior of photo-responsive system composed of 1-hexadecyl-3-methylimidazolium bromide and 2-methoxycinnamic acid, *RSC Adv.*, 2015, **5**, 68369–68377.

40 E. Van Lenthe and E. J. Baerends, Optimized slater-type basis sets for the elements 1-118, *J. Comput. Chem.*, 2003, **24**, 1142–1156.

41 D. Van der Spoel, E. Lindahl, B. Hess, G. Groenhof, A. E. Mark and H. J. C. Berendsen, GROMACS: Fast, flexible, and free, *J. Comput. Chem.*, 2005, **26**, 1701–1718.

© 2023 The Author(s). Co-published by the Institute of Process Engineering, Chinese Academy of Sciences and the Royal Society of Chemistry

Ind. Chem. Mater., 2023, **1**, 262–270 | **269**

42 T. Darden, D. York and L. Pedersen, Particle mesh Ewald: An N.Log(N) method for Ewald sums in large systems, *J. Chem. Phys.*, 1993, **98**, 10089–10092.

43 L. Martinez, R. Andrade, E. G. Birgin and J. M. Martinez, PACKMOL: A package for building initial configurations for molecular dynamics simulations, *J. Comput. Chem.*, 2009, **30**, 2157–2164.

44 J. N. C. Lopes, J. Deschamps and A. A. H. Padua, Modeling ionic liquids using a systematic all-atom force field, *J. Phys. Chem. B*, 2004, **108**, 2038–2047.

45 A. S. L. Gouveia, C. E. S. Bernardes, L. C. Tome, E. I. Lozinskaya, Y. S. Vygodskii, A. S. Shaplov, J. N. C. Lopes and I. M. Marrucho, Ionic liquids with anions based on fluorosulfonyl derivatives: from asymmetrical substitutions to a consistent force field model, *Phys. Chem. Chem. Phys.*, 2017, **19**, 29617–29624.

46 J. N. C. Lopes and A. A. H. Padua, Molecular force field for ionic liquids III: Imidazolium, pyridinium, and phosphonium cations; Chloride, bromide, and dicyanamide anions, *J. Phys. Chem. B*, 2006, **110**, 19586–19592.

47 K. I. Oh, J. H. Choi, J. H. Lee, J. B. Han, H. Lee and M. Cho, Nitrile and thiocyanate IR probes: Molecular dynamics simulation studies, *J. Chem. Phys.*, 2008, **128**, 154504–154514.

48 W. L. Jorgensen, D. S. Maxwell and J. TiradoRives, Development and testing of the OPLS all-atom force field on conformational energetics and properties of organic liquids, *J. Am. Chem. Soc.*, 1996, **118**, 11225–11236.